Single-molecule force stability of the SARS-CoV-2–ACE2 interface in variants-of-concern

Magnus S. Bauer ●[1,2,3,4,8], Sophia Gruber[1,8], Adina Hausch ●[1,5,8], Marcelo C. R. Melo ●[6,8], Priscila S. F. C. Gomes ●[6,8], Thomas Nicolaus[1], Lukas F. Milles ●[3,4], Hermann E. Gaub[1,9], Rafael C. Bernardi ●[6,9] & Jan Lipfert ●[1,7,9] ✉

Mutations in SARS-CoV-2 have shown effective evasion of population immunity and increased affinity to the cellular receptor angiotensin-converting enzyme 2 (ACE2). However, in the dynamic environment of the respiratory tract, forces act on the binding partners, which raises the question of whether not only affinity but also force stability of the SARS-CoV-2–ACE2 interaction might be a selection factor for mutations. Using magnetic tweezers, we investigate the impact of amino acid substitutions in variants of concern (Alpha, Beta, Gamma and Delta) and on force-stability and bond kinetic of the receptor-binding domain–ACE2 interface at a single-molecule resolution. We find a higher affinity for all of the variants of concern (>fivefold) compared with the wild type. In contrast, Alpha is the only variant of concern that shows higher force stability (by 17%) compared with the wild type. Using molecular dynamics simulations, we rationalize the mechanistic molecular origins of this increase in force stability. Our study emphasizes the diversity of contributions to the transmissibility of variants and establishes force stability as one of the several factors for fitness. Understanding fitness advantages opens the possibility for the prediction of probable mutations, allowing a rapid adjustment of therapeutics, vaccines and intervention measures.

Viruses constantly adapt to their hosts through genomic changes. Although many mutations are silent or inviable, some result in increased fitness by increasing the intrinsic transmissibility or evasion of population immunity. Better adaptation and higher transmissibility enable new variants to supersede existing ones, as it was observed by the emergence and rapid spread of variants of concern (VOCs) of SARS-CoV-2 (Supplementary Fig. 1). Adaptations associated with the increased fitness of SARS-CoV-2 often go along with higher affinity to host factors[1–4]. Nonetheless, the attachment of SARS-CoV-2 to the human angiotensin-converting enzyme 2 (ACE2) receptor occurs within the dynamic environment of the respiratory tract, where external forces generated by breathing, coughing and ciliary-beating-mediated mucus
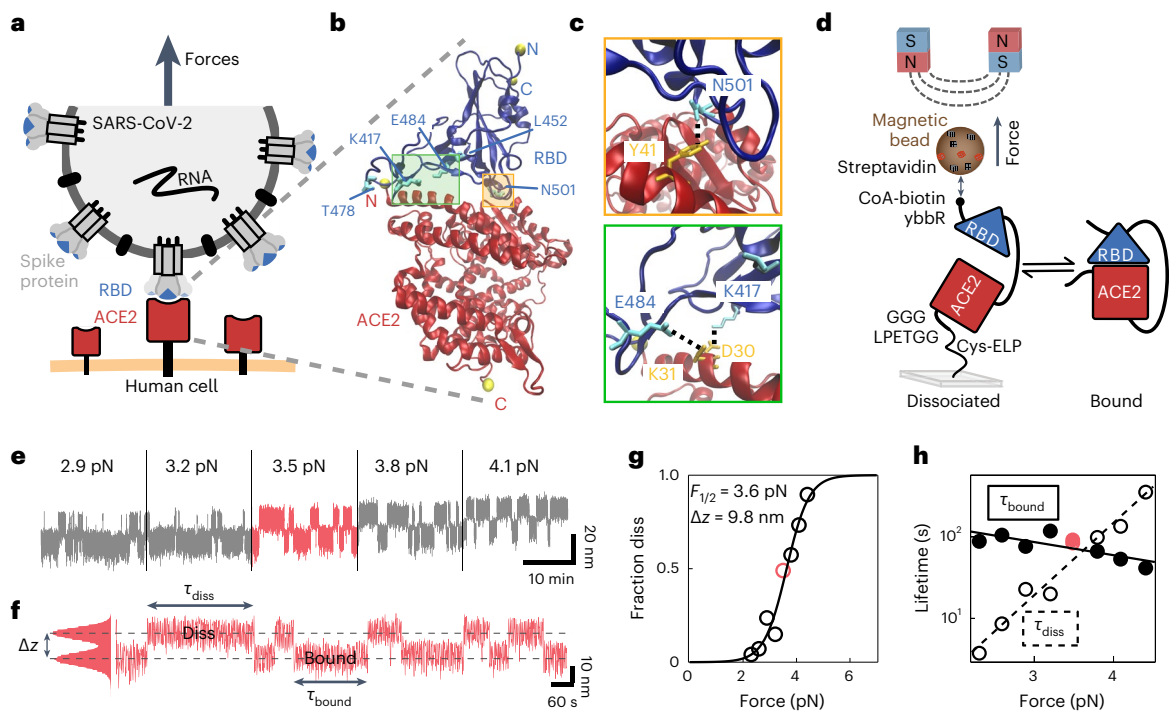
Fig. 1 | A single-molecule tethered ligand assay to study RBD binding to ACE2 for VOCs of SARS-CoV-2. a, A SARS-CoV-2 virion (grey) presents its spike protein trimers containing three RBDs (blue) ready for binding to human ACE2 (red). Attachment occurs in the dynamic environment of the respiratory tract, where the interaction must withstand external forces (black arrow). **b**, Crystal structure of SARS-CoV-2 RBD (blue) bound to ACE2 (red) (PDB ID: 6m0j)[1]. The termini of protein chains are marked with yellow spheres. Amino acid substitutions featured in current VOCs are indicated in cyan. The crystal structure was rendered using VMD[2]. **c**, Zoomed-in views of the interface regions indicated in **b**. RBD residue N501 featured in VOCs Alpha, Beta and Gamma forms a hydrogen bond with ACE2 residue Y41 (top)[1]. RBD residues E484 and K417 featured in VOCs Beta and Gamma form salt bridges and hydrogen bonds with ACE2 residues K31 and D30, respectively (bottom)[1,3]. Bridges and bonds are indicated by the black dashed lines. **d**, Schematic of the tethered ligand construct in MT. SARS-

CoV-2 RBD (blue) is tethered via a flexible peptide linker to ACE2 (red). The construct is covalently attached to the glass surface via an ELP linker (Methods) and to a streptavidin-covered magnetic bead via biotin at the C terminus of the protein construct. **e**, Representative extension time trace of the tethered ligand construct in MT shows the binding and dissociation of the SARS-CoV-2 RBD–ACE2 interaction at plateaus of constant force. With increasing force, the interface is predominantly dissociated. **f**, Segment of the trace in **e** at 3.5 pN, where it is equally distributed between the bound and dissociated ('diss') state. The fraction dissociated at this force is, thus, 0.5. Lifetimes in the dissociated state (τ_{diss}) and in the bound state (τ_{bound}) are indicated. **g**, Fraction dissociated as a function of the applied force (circles) and fit of a two-state model (solid line), with $F_{1/2}$ and Δz (inset) as the fitting parameters. **h**, Mean lifetimes in the bound and dissociated states for the molecule shown in **e–g** as a function of force (circles) and fit with an exponential model (solid lines).

clearing[5,6] continuously challenge the attachment process (Fig. 1a). It is crucial to recognize that for a successful infection, not only affinity but also stability under force of the viral attachment to the host play a critical role[7–15]. Single-molecule measurements and molecular dynamics (MD) simulations have investigated the mechanical stability of SARS-CoV-2 binding to its receptor ACE2 (refs. 2,11–13,16–19). In particular, single-molecule measurements have demonstrated that SARS-CoV-2 VOCs exhibit higher binding frequencies[11,13,16], greater avidity[17] and extended bound lifetimes[11,13,17] compared to the wild-type (wt) virus, suggesting differences in mechanical stability among variants.

Despite these findings, the variation in force stability across various VOCs and its potential correlation with viral transmissibility remain unclear. In this study, we employ a highly sensitive single-molecule assay designed to simulate the natural force exposure experienced during infection, enabling the examination of SARS-CoV-2 attachment to ACE2 under load. Our approach uses a fusion protein construct that features the receptor-binding domain (RBD) from the SARS-CoV-2 spike protein coupled to the ACE2 ectodomain via a flexible peptide linker with molecular handles suitable for attachment in magnetic tweezers (MT) (Fig. 1b–d)[18]. Coupling in MT enables us to probe the mechanical strength and dynamics of the RBD–ACE2 interaction under precisely defined forces, with a very high force resolution[18–24] (Fig. 1). Using our single-molecule assay, we characterize the interaction of SARS-CoV-2 wt and VOC constructs with ACE2. Our assay enables

the direct measurements of force stability and reveals significant differences between the VOCs. Furthermore, we are able to identify the amino acid substitutions responsible for the changes. In addition to force stability, we find that by extrapolating bond lifetimes to zero force, we can quantitatively compare with and reproduce equilibrium affinity constants measured in bulk. Using MD simulations, we identify key residues that stabilize the RBD–ACE2 interface and calculate the correlation between their movements. Aggregating the individual correlations from MD simulations into a new total correlation metric, we are able to accurately reproduce the experimentally determined relations in force stabilities. Thus, we can experimentally determine differences in force stability between different VOCs using MT and elucidate their molecular origin with the help of MD simulations. Correlating our results to observations from epidemiology, we suggest that increased force stability of the ACE2:RBD interface can increase the intrinsic transmissibility. We anticipate that taking into account force stability will aid the predictions of future VOCs.

Results and discussion

Force stability of SARS-CoV-2 interaction with ACE2 for VOCs

We design fusion protein constructs comprising the ectodomain of the human ACE2 receptor connected by a flexible polypeptide linker to the RBD of SARS-CoV-2 for both the wt strain and Alpha, Beta, Gamma and Delta VOCs (Fig. 1c,d and Table 1). We attach the tethered ligand

Table 1 | VOCs compared with SARS-CoV-2 wt

WHO name	PANGO lineage	Country of first observation	AA changes in RBD	$F_{1/2}$ (pN) $(F_{1/2}/F_{1/2}(wt))>1$: higher force stability than wt	$\tau_{0,diss}$ (s) $(t_{0,diss}/t_{0,diss}(wt))<1$: faster binding than wt at $F=0$	$\tau_{0,bound}$ (s) $(t_{0,bound}/t_{0,bound}(wt))>1$: slower dissociation than wt at $F=0$	K_D $(K_D/K_D(wt))<1$: higher affinity than wt
wt	A	–	–	3.8±0.4 (1)	0.06±0.17 (1)	121±284 (1)	$532×10^{-6}$ (1)
Alpha	B1.1.7	UK	N501Y	4.5±0.3 (1.17)	0.01±0.02 (0.22)	464±740 (3.82)	$30×10^{-6}$ (0.06)
Beta	B1.1.351	South Africa	N501Y E484K K417N	3.8±0.3 (1.01)	0.02±0.06 (0.37)	218±315 (1.79)	$110×10^{-6}$ (0.21)
Gamma	P1	Brazil	N501Y E484K K417T	4.0±0.6 (1.06)	0.02±0.04 (0.27)	552±1,178 (4.55)	$31×10^{-6}$ (0.06)
Delta	B1.617.2	India	L452R T478K	3.8±0.3 (1.00)	0.01±0.02 (0.18)	427±707 (3.52)	$27×10^{-6}$ (0.05)

Number of molecules: 13 molecules (wt), 11 molecules (Alpha), 10 molecules (Beta), 14 molecules (Gamma), 20 molecules (Delta).

constructs to a glass surface and a magnetic bead using a previously established protocol based on specific peptide linkers[18–20,25]. Using MT, we probe the stability of the RBD–ACE2 interaction at varying levels of constant forces (Supplementary Fig. 2). At high forces (larger than 25 pN), ACE2 unfolds with a characteristic unfolding signature, which we use for each molecular construct probed in the MT to identify specific tethers (Supplementary Figs. 3 and 4). At forces below 10 pN, where both protein domains are folded, the linker ensures that the receptor and ligand remain in proximity on dissociation, allowing them to re-bind[18,26–30]. We can, thus, study repeated (re-)binding and dissociation of the same SARS-CoV-2 RBD and ACE2 interaction under different forces (Fig. 1e). At low forces (<2 pN), we find the bond to be predominantly formed, whereas increasing the force leads to elongated periods where the binding partners are dissociated. Quantifying the force dependence of the RBD–ACE2 interaction gives access to both equilibrium force stability and dynamics of interactions.

To characterize the force stability, and to particularly compare it across the different VOCs, we use $F_{1/2}$, the midpoint force, at which it is equally probable to find the tethered ligand system in the bound or dissociated conformation (Fig. 1f). We determine $F_{1/2}$ by fitting a two-state model to the fraction dissociated (f_{diss}) as a function of force (Fig. 1g):

$$f_{diss}(F) = \frac{1}{(1 + \exp(-\Delta z(F - F_{\frac{1}{2}})/k_B T))} \qquad (1)$$

where k_B is Boltzmann's constant and T is the absolute temperature. $F_{1/2}$ and Δz are fitting parameters that represent the midpoint force and the distance between the two states along the pulling direction, respectively. The dissociated fraction is calculated for each plateau of constant force by dividing the time spent in the dissociated conformation by the total plateau time. Comparing $F_{1/2}$ for the wt and different VOCs, using otherwise identical constructs (Fig. 2a,b and Supplementary Figs. 5 and 6), we find that the force stability for the Alpha VOC is highly significantly larger than wt ($p = 5.2 \times 10^{-4}$, two-tailed t-test). In contrast, we observe no statistically significant difference between SARS-CoV-2 wt and Beta ($p > 0.80$), wt and Gamma ($p > 0.26$) or wt and Delta ($p > 0.99$). In addition to the naturally emerged VOCs, we tested individual amino acid substitutions and found that E484K slightly lowers $F_{1/2}$, although not statistically significantly, whereas K417N lowers the force stability highly significantly ($p = 4.5 \times 10^{-5}$).

Dynamics of the RBD–ACE2 interactions
To characterize the dynamics of the interactions, we determine the lifetimes of the dissociated and bound states as a function of force. The lifetime distributions are well described by single exponentials (Supplementary Fig. 8). The resulting mean lifetimes, namely, τ_{diss}

and τ_{bound} (Fig. 1h, circles), exhibit an exponential force dependence (Fig. 1h, lines). The intersection of the fitted lifetimes in the dissociated and bound states provides an alternative route to determine the midpoint force $F_{1/2}$ and we find excellent agreement in both absolute values and differences across VOCs with the $F_{1/2}$ values determined using the two-state model (equation (1) and Supplementary Table 1).

Further, extrapolation of the fits to zero force, assuming a slip-bond behaviour with an exponential dependence of lifetime on force, yields lifetimes of the bond in the absence of force (Fig. 2c and Supplementary Table 1). The lifetimes of the dissociated state rapidly increase with increasing force for all constructs, which is expected as the peptide linker extends under force, which, in turn, impedes bond re-formation[18,26,31,32]. Conversely, the lifetimes of the bound state τ_{bound} decrease with force for all VOCs. However, the force dependence of τ_{bound} differs for the different VOCs (Supplementary Fig. 7). For Alpha, we find a higher τ_{bound} than for wt over the whole measured force range (Fig. 2c), again indicating a higher force stability of Alpha in this force range, in line with the observation of a higher $F_{1/2}$ for Alpha. The other VOCs exhibit overall similar lifetimes in the bound state compared with wt under force, in line with their similar $F_{1/2}$ values.

Bond lifetimes at zero force predict affinities
The force dependence of the bond lifetime (that is, the slope shown in Fig. 2c) considerably varies across the VOCs, leading to very different extrapolated lifetimes $\tau_{0,bound}$ and $\tau_{0,diss}$ in the absence of a load. The lifetimes at zero force can be related to affinities: the ratio $\tau_{0,diss}/\tau_{0,bound}$ (or equivalently the ratio of the rates $k_{0,off}/k_{0,on}$, which are the inverses of the lifetimes) define unimolecular equilibrium constants for the tethered ligand system $K_D^{TL} = \tau_{0,diss}/\tau_{0,bound}$ (Supplementary Fig. 9). The K_D^{TL} values are dimensionless, since both on and off rates for the tethered ligand systems are in units of s^{-1}. To compare K_D^{TL} to bulk binding measurements, we need to take into account that in standard solution assays, without a linker, the bimolecular equilibrium constant $K_{D,sol} = k_{off,sol}/k_{on,sol}$ has units of molar (M), since although the off rate $k_{off,sol}$ is directly comparable with $k_{0,off}$, the on rate $k_{on,sol}$ depends on the ligand concentration, with the units of $M^{-1} s^{-1}$.

Therefore, we normalize both unimolecular equilibrium constant K_D^{TL} and bimolecular dissociation constants $K_{D,sol}$ obtained using standard binding assays[1–9,33–37] to the wt and compare across the VOCs (Fig. 2d). We find good agreement between the affinities determined in our single-molecule assay by extrapolation to zero force and the values obtained from standard affinity measurements (Fig. 2d). The good agreement between bulk affinity measurements in the absence of force and values from our assay suggest that our constant-force MT measurements are close enough to equilibrium to probe the same (or at least a sufficiently similar) binding pathway as the free solution measurements. The exponential decrease in the lifetime of the bound
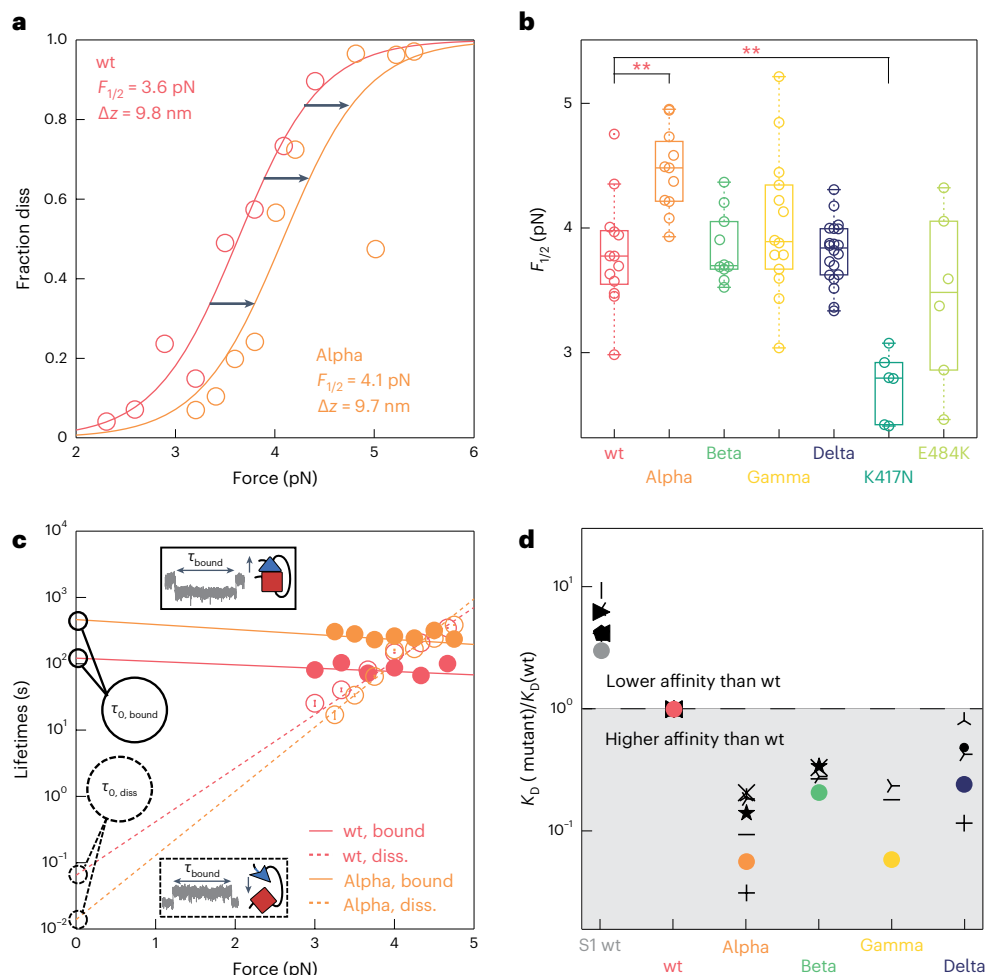
Fig. 2 | Effects of VOCs on interface force stability and affinity.
a, Representative force-dependent fraction dissociated for one single wt
(red), and one Alpha (orange) tethered ligand construct. The points represent
experimental data and the solid lines are two-state fits. Supplementary Fig.
5 presents additional data. **b**, Midpoint forces determined for wt, VOCs and
K417N, and E484K single amino acid substitutions. $F_{1/2}$ of Alpha and K417N
deviate highly significantly from wt ($p = 0.00052$ and $p = 0.000045$, respectively)
using a two-sided t-test without adjustments for multiple comparisons. Beta,
Gamma, Delta and E484K show no statistically significant difference to the
wt. A bootstrap analysis revealed similar significance levels for the different
variants (Supplementary Fig. 6). Individual points are derived from independent
molecules. Centre line, bottom and top of the boxes indicate the median and

the 25th and 75th percentile, respectively. Supplementary Table 1 provides
the numerical data. **c**, Force-dependent lifetimes (circles) and fits to the data
in the bound (solid lines) and dissociated (dashed) states of wt and Alpha.
Individual points are the means of lifetimes observed for a single molecule at a
given force. The insets show the example lifetimes in MT traces. Supplementary
Fig. 7 shows additional comparisons for the other VOCs. **d**, Mean dissociation
constant normalized to the wt (K_D/K_D(wt); Supplementary Fig. 9 shows the
un-normalized K_D values) determined from our measurements (coloured dots)
and compared with previous traditional bulk affinity measurements (SPR or
BLI)[3–9] (Supplementary Table 2). Statistics in **b** and **c** reflect 13 molecules (wt), 11
molecules (Alpha), 10 molecules (Beta), 14 molecules (Gamma), 20 molecules
(Delta), 6 molecules (E484K) and 6 molecules (K417N).

state with increasing force (Fig. 2c) and the good agreement between
the force spectroscopy data extrapolated to zero force and the bulk
binding measurements also imply that the RBD–ACE2 interaction is not
a catch bond, but a 'regular' slip bond, which weakens under increasing
force. However, the data also reveal a clear difference between affinities
at zero force and stability under a mechanical load: although all VOCs
exhibit increased affinity compared with wt, only Alpha shows a higher
force stability. A clear difference between force stability and thermo-
dynamic affinity has been seen for a range of molecular bonds[38,39] and
our findings suggest that force stability must be taken into account as
an independent factor when assessing VOCs.

Molecular basis of different force stabilities across VOCs
To provide a microscopic understanding of the observed differences in
force stability, we performed all-atom MD simulations of the different
RBD–ACE2 complexes. The structures of the VOCs were obtained by

comparative modelling using MODELLER[40], taking the SARS-CoV-2 wt
structure as the template[18]. For each system, five replicas were simu-
lated for a total of 1.0 μs using NAMD 3.0 (ref. 41). Trajectories were
analysed with VMD[30] and dynamical network analysis[42], which meas-
ure the correlation between the motions of neighbouring residues to
determine how cooperative their motion is. The higher the correlation
between residues, the more relevant is their interaction for the stabil-
ity of the protein complex[43]. We determined contacts by tracking the
distance between neighbouring residues throughout the simulations
and then selected the contacts with the highest correlation for further
analysis (Supplementary Fig. 10). Using these selection criteria, we iden-
tify the main contacts that are responsible for stabilizing the RBD–ACE2
complex (Fig. 3a,b,c) and would, thus, be expected to have the greatest
impact on force stability. All residues selected by the contact criterion
in the network analysis are found within the receptor-binding-motif
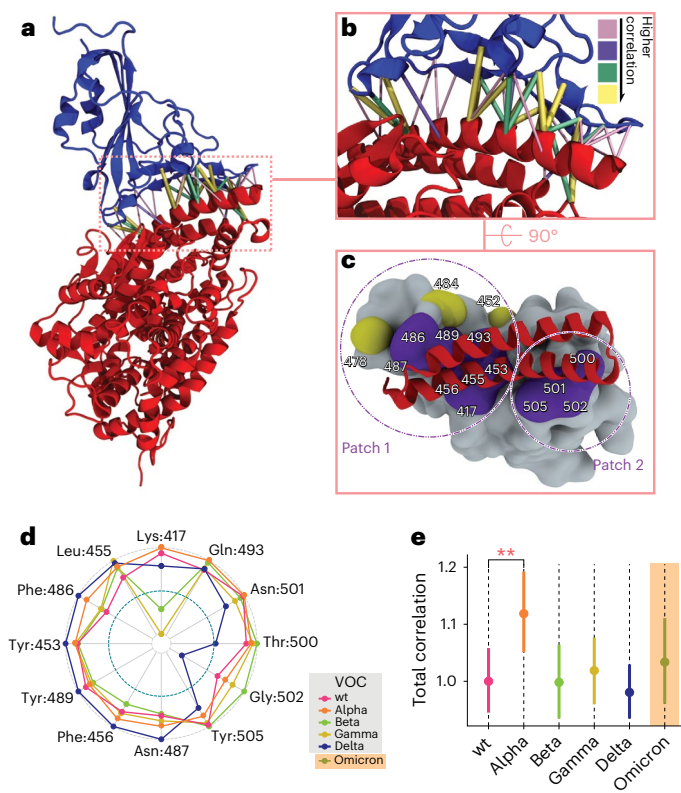(residues N437 to Y508) region, at the RBD–ACE2 interface, defined

Fig. 3 | Effects of VOCs on the contact network at the RBD–ACE2 interface.
a, Network interactions between spike RBD (blue) in complex with ACE2 (red) of an exemplary MD trajectory represented as colour-coded cylinders according to their correlation, where thicker cylinders in yellow and green represent highly correlated residues. Less-correlated residues are depicted in light and dark purple and thin lines. **b**, Zoomed-in views of the structure shown in **a**, focusing on the RBD–ACE2 interface. **c**, Detailed RBD–ACE2 interfacial surface, highlighting the RBD in grey and ACE2 helices in red. The residues coloured in violet are highly correlated, whereas the residues coloured in yellow are less correlated. **d**, Total correlations for selected residues for the different VOCs. The values are normalized to the VOC with the strongest correlation. **e**, Total correlation of motion summarized from the dynamic network interactions of all of the main correlations across the RBD–ACE2 interface, for each VOC. A total of 75 windows per VOC ($n = 75$) were used to calculate their total correlation. The total correlation measurements for all variants were normalized by the mean total correlation in the wt. The bars represent the 90% CIs for the mean. The Alpha VOC shows a significantly higher correlation than wt ($p = 0.04$). All other VOCs are not significantly different from wt. Significance was assessed using the non-parametric bootstrapping technique for hypothesis testing. Supplementary Fig. 13 shows additional significance tests via bootstrapping.

as the 4 Å cut-off based on the PDB ID 6m0j crystal structure[44] (Supplementary Fig. 11 shows the individual correlations). The total sum of correlations for RBD residues (Fig. 3d and Supplementary Fig. 10) mostly highlights hydrophobic residues as well as residues that are not mutated in the VOCs, revealing that stabilizing the bond between RBD–ACE2 involves an interplay of different interactions. Mutations in the VOCs lead to a rebalancing of interactions with ACE2, losing correlation in some regions whereas gaining in others (Fig. 3d and Supplementary Fig. 10).

Examining the specific mutations involved in the VOCs, we can rationalize the observed differences in force stability. Alpha carries only one substitution in the RBD, namely, N501Y, which is also present in Beta and Gamma. The N501Y substitution creates an additional hydrogen bond and leads to increased π-stacking with residue Y41 of ACE2 (ref. 45), which increases the pairwise correlation (Supplementary Figs. 11

and 12) and enhances the correlations in the vicinity of position N501, particularly at residues T500 and G502 (Fig. 3d).

The Beta and Gamma VOCs feature, in addition to N501Y, amino acid substitutions at position K417N/T and E484K. In the wt, the residues K417 and E484 form salt bridges with residues D30 and K31 of ACE2, respectively[1,3]. Due to a charge reversal in the case of E484K and a charge removal in the case of K417N (Beta) and K417T (Gamma), these salt bridges are disrupted. The disruption of the salt bridge at position 417 leads to a dramatic loss in correlation (Fig. 3d), fully in line with a dramatically decreased force stability for K417N (Fig. 2b). The charge reversal by mutation E484K leads to the loss of the salt bridge with K31, which is, however, compensated by an alternative salt bridge with E35 (ref. 3). As a result, the correlations around position E484 are virtually unaffected by the mutation (for example, residues F486, N487 and Y489; Fig. 3d), consistent with only a slight and statistically insignificant decrease in $F_{1/2}$ for the E484K mutation (Fig. 2b). In summary, for the Beta and Gamma VOCs, the increased force stability by N501Y is offset by the reduction in stability, particularly by K417N/T, such that the total effect is a similar force stability as wt.

The mutations in the Delta VOC, L452R and T478K, are located further away from the RBD–ACE2 interface, and there are no direct interactions involving these residues. Nonetheless, the Delta mutations do shift the correlation pattern, with correlations in the 'Patch 2' region (Fig. 3c) around position N501 decreasing and increasing in 'Patch 1' around P479.

To summarize the contact network and the correlations of motion in a single metric to provide an overall measure of mechanical stability and to directly compare with the experimental force stability measurements, we define the total correlation as the sum of all correlations between stable contacts identified through the network analysis. We simulate the wt, the experimentally examined VOCs and the more recently emerged Omicron VOC, and compute the total correlation scores using a bootstrapping approach to determine the confidence intervals (CIs) (Fig. 3e and Supplementary Fig. 13). We find excellent agreement between the total correlation metric and the experimentally determined values for the force stability assessed by $F_{1/2}$: wt, Beta, Gamma and Delta exhibit the same force stabilities, whereas Alpha has a statistically larger $F_{1/2}$ and total correlation. Interestingly, the recent Omicron variant, which features a very large number of mutations (15 in the RBD alone[46]), has a total correlation value between Alpha and the wt, and did not show statistically significant differences when compared with Alpha and wt.

Discussion

We have used our tethered ligand assay and exploited the high sensitivity of MT and their ability to measure at constant forces to precisely determine both force stability and affinity of different SARS-CoV-2 VOCs binding to ACE2. Unlike traditional bulk affinity measurements, our assay provides additional insights into bond stability and kinetics under a mechanical load, mimicking the natural binding circumstances in the dynamic environment of the respiratory tract. We find that although the Alpha, Beta, Gamma and Delta VOCs have increased affinities to ACE2 compared with wt, only Alpha has a higher force stability. This is in contrast to atomic force microscopy (AFM) measurements, which have reported the same rupture forces, within experimental error, for different VOCs[13], or slightly higher forces for either Delta[16] or for both Alpha and Beta compared with wt[11], without reporting the statistical significance. The differences between the AFM results and our MT findings might be due to the much higher loading rate of the AFM measurements, probing a different dissociation pathway or due to the lower force resolution of AFM measurements in the low-force regime[23,47]. We note that extrapolated lifetimes in the bound configuration from the AFM measurements are lower for wt than for Alpha, Beta, Gamma, Delta and Omicron[11,13,17], consistent with our findings.

Viral fitness depends on multiple factors, including cleavage and cell entry, replication, and viral packing and release[48–53]. Correspondingly, the VOCs carry mutations in positions beyond the RBD. However, attachment to the host cell is a critical first step in viral infection and it is instructive to relate trends observed epidemiologically with our findings about the RBD–ACE2 interaction. The Alpha, Beta and Gamma VOCs emerged in the second half of 2020 and began to widely circulate in late 2020 and early 2021 (Supplementary Fig. 1). In Europe and Northern America, Alpha, but not Beta or Gamma, quickly replaced the wt and became the dominant circulating variant (Supplementary Fig. 1). At that time, there was no widespread population immunity in Northern America or Europe (Supplementary Fig. 1), suggesting that Alpha, but not Beta or Gamma, has a significant advantage in a (largely) immune-naïve population[54]. We speculate that the higher force stability of Alpha contributes to its epidemiologically observed higher transmissibility compared with wt, Beta or Gamma. The Beta and Gamma variants became dominant in South Africa and Brazil (Supplementary Fig. 1), in a setting where there was already significant population immunity through natural infections[55,56]. The charge-change mutations at positions K417 and E484 present in Beta and Gamma reduce the binding of certain neutralizing antibodies[57–59], but lower the force stability. Consequently, the Beta and Gamma appear to confer an advantage to the virus in populations with significant immunity, but not in an immune-naïve population. The Delta and Omicron VOCs became dominant globally in mid-2021 and early 2022, respectively, at a time where there was significant population immunity through vaccinations as well as natural infections (Supplementary Fig. 1). Both variants show immune escape[37,60–62] and probably enhanced transmission through substitution at the S1/S2 cleavage site, yet no or only slightly increased force stability (Fig. 2b,d)[63–65]. These observations raise the possibility that a new variant might emerge that combines the fitness advantages present in Omicron with a higher force stability, which could make it even more transmissible. Our correlation-based analysis of the RBD–ACE2 interface by MD simulations and high-resolution force spectroscopy measurements of the interface in the tethered ligand assay has the potential to help understand and ultimately predict the spread of SARS-CoV-2 variants.

Online content

Any methods, additional references, Nature Portfolio reporting summaries, source data, extended data, supplementary information, acknowledgements, peer review information; details of author contributions and competing interests; and statements of data and code availability are available at https://doi.org/10.1038/s41565-023-01536-7.

References

1. Laffeber, C., Koning, K. D., Kanaar, R. & Lebbink, J. H. G. Experimental evidence for enhanced receptor binding by rapidly spreading SARS-CoV-2 variants. *J. Mol. Biol.* **433**, 167058–167058 (2021).
2. Barton, M. I. et al. Effects of common mutations in the SARS-CoV-2 spike RBD and its ligand, the human ACE2 receptor on binding affinity and kinetics. *eLife* **10**, e70658 (2021).
3. Majumdar, P. & Niyogi, S. SARS-CoV-2 mutations: the biological trackway towards viral fitness. *Epidemiol. Infect.* **149**, E110 (2021).
4. Bayarri-Olmos, R. et al. The alpha/B.1.1.7 SARS-CoV-2 variant exhibits significantly higher affinity for ACE-2 and requires lower inoculation doses to cause disease in K18-hACE2 mice. *eLife* **10**, e70002 (2021).
5. Hill, D. B. et al. Force generation and dynamics of individual cilia under external loading. *Biophys. J.* **98**, 57–66 (2010).
6. Wu, C.-T. et al. SARS-CoV-2 replication in airway epithelia requires motile cilia and microvillar reprogramming. *Cell* **186**, 112–130.e20 (2023).
7. Milles, L. F., Schulten, K., Gaub, H. E. & Bernardi, R. C. Molecular mechanism of extreme mechanostability in a pathogen adhesin. *Science* **359**, 1527–1533 (2018).
8. Alsteens, D. et al. Nanomechanical mapping of first binding steps of a virus to animal cells. *Nat. Nanotechnol.* **12**, 177–183 (2017).
9. Koehler, M., Delguste, M., Sieben, C., Gillet, L. & Alsteens, D. Initial step of virus entry: virion binding to cell-surface glycans. *Annu. Rev. Virol.* **7**, 143–165 (2020).
10. Sokurenko, E. V., Vogel, V. & Thomas, W. E. Catch-bond mechanism of force-enhanced adhesion: counterintuitive, elusive, but...widespread? *Cell Host Microbe* **4**, 314–323 (2008).
11. Tian, F. et al. N501Y mutation of spike protein in SARS-CoV-2 strengthens its binding to receptor ACE2. *eLife* **10**, e69091 (2021).
12. Zheng, Bin, et al. S373P mutation stabilizes the receptor-binding domain of the spike protein in omicron and promotes binding. *JACS Au* https://doi.org/10.1021/jacsau.3c00142 (2023).
13. Koehler, M. et al. Molecular insights into receptor binding energetics and neutralization of SARS-CoV-2 variants. *Nat. Commun.* **12**, 6977 (2021).
14. Yang, J. et al. Molecular interaction and inhibition of SARS-CoV-2 binding to the ACE2 receptor. *Nat. Commun.* **11**, 4541 (2020).
15. Cao, W. et al. Biomechanical characterization of SARS-CoV-2 spike RBD and human ACE2 protein-protein interaction. *Biophys. J.* **120**, 1011–1019 (2021).
16. Zhang, X. et al. Pathogen-host adhesion between SARS-CoV-2 spike proteins from different variants and human ACE2 studied at single-molecule and single-cell levels. *Emerging Microbes Infect.* **11**, 2658–2669 (2022).
17. Zhu, R. et al. Force-tuned avidity of spike variant-ACE2 interactions viewed on the single-molecule level. *Nat. Commun.* **13**, 7926 (2022).
18. Bauer, M. S. et al. A tethered ligand assay to probe SARS-CoV-2:ACE2 interactions. *Proc. Natl Acad. Sci. USA* **119**, e2114397119 (2022).
19. Bauer, M. S. et al. A tethered ligand assay to probe the SARS-CoV-2 ACE2 interaction under constant force. Preprint at *biorxiv* https://doi.org/10.1101/2020.09.27.315796 (2020).
20. Löf, A. et al. Multiplexed protein force spectroscopy reveals equilibrium protein folding dynamics and the low-force response of von Willebrand factor. *Proc. Natl Acad. Sci. USA* **116**, 18798–18807 (2019).
21. Lansdorp, B. M. & Saleh, O. A. Power spectrum and Allan variance methods for calibrating single-molecule video-tracking instruments. *Rev. Sci. Instrum.* **83**, 025115 (2012).
22. Velthuis, A. J. W. T., Kerssemakers, J. W. J., Lipfert, J. & Dekker, N. H. Quantitative guidelines for force calibration through spectral analysis of magnetic tweezers data. *Biophys. J.* **99**, 1292–1302 (2010).
23. Neuman, K. C. & Nagy, A. Single-molecule force spectroscopy: optical tweezers, magnetic tweezers and atomic force microscopy. *Nat. Methods* **5**, 491–505 (2008).
24. Lipfert, J., Hao, X. & Dekker, N. H. Quantitative modeling and optimization of magnetic tweezers. *Biophys. J.* **96**, 5040–5049 (2009).
25. Ott, W. et al. Elastin-like polypeptide linkers for single-molecule force spectroscopy. *ACS Nano* **11**, 6346–6354 (2017).
26. Kim, J., Zhang, C. Z., Zhang, X. & Springer, T. A. A mechanically stabilized receptor-ligand flex-bond important in the vasculature. *Nature* **466**, 992–995 (2010).
27. Shrestha, P. et al. Single-molecule mechanical fingerprinting with DNA nanoswitch calipers. *Nat. Nanotechnol.* **16**, 1362–1370 (2021).
28. Yang, D., Ward, A., Halvorsen, K. & Wong, W. P. Multiplexed single-molecule force spectroscopy using a centrifuge. *Nat. Commun.* **7**, 11026 (2016).

29. Kilchherr, F. et al. Single-molecule dissection of stacking forces in DNA. *Science* **353**, aaf5508 (2016).

30. Le, S., Yu, M. & Yan, J. Direct single-molecule quantification reveals unexpectedly high mechanical stability of vinculin—talin/α-catenin linkages. *Sci. Adv.* **5**, eaav2720 (2019).

31. Halvorsen, K., Schaak, D. & Wong, W. P. Nanoengineering a single-molecule mechanical switch using DNA self-assembly. *Nanotechnology* **22**, 494005 (2011).

32. Kostrz, D. et al. A modular DNA scaffold to study protein-protein interactions at single-molecule resolution. *Nat. Nanotechnol.* **14**, 988–993 (2019).

33. Gong, S. Y. et al. Contribution of single mutations to selected SARS-CoV-2 emerging variants spike antigenicity. *Virology* **563**, 134–145 (2021).

34. Rajah, M. M. et al. SARS-CoV-2 Alpha, Beta, and Delta variants display enhanced spike-mediated syncytia formation. *EMBO J.* **40**, e108944 (2021).

35. Gobeil, S. M. C. et al. Effect of natural mutations of SARS-CoV-2 on spike structure, conformation, and antigenicity. *Science* **373**, eabi6226 (2021).

36. Ren, W. et al. Characterization of SARS-CoV-2 variants B.1.617.1 (Kappa), B.1.617.2 (Delta), and B.1.618 by cell entry and immune evasion. *mBio* **13**, e00099–00022 (2022).

37. McCallum, M. et al. Molecular basis of immune evasion by the Delta and Kappa SARS-CoV-2 variants. *Science* **374**, 1621–1626 (2021).

38. Albrecht, C. et al. DNA: a programmable force sensor. *Science* **301**, 367–370 (2003).

39. Gruber, S. et al. Designed anchoring geometries determine lifetimes of biotin–streptavidin bonds under constant load and enable ultra-stable coupling. *Nanoscale* **12**, 21131–21137 (2020).

40. Webb, B. & Sali, A. Comparative protein structure modeling using MODELLER. *Curr. Protoc. Bioinform* **54**, 5.6.1–5.6.37 (2016).

41. Phillips, J. C. et al. Scalable molecular dynamics on CPU and GPU architectures with NAMD. *J. Chem. Phys.* **153**, 044130 (2020).

42. Melo, M. C. R., Bernardi, R. C., Fuente-Nunez, C. D. L. & Luthey-Schulten, Z. Generalized correlation-based dynamical network analysis: a new high-performance approach for identifying allosteric communications in molecular dynamics trajectories. *J. Chem. Phys.* **153**, 134104 (2020).

43. Schoeler, C. et al. Mapping mechanical force propagation through biomolecular complexes. *Nano Lett.* **15**, 7370–7376 (2015).

44. Lan, J. et al. Structure of the SARS-CoV-2 spike receptor-binding domain bound to the ACE2 receptor. *Nature* **581**, 215–220 (2020).

45. Liu, H. et al. The basis of a more contagious 501Y.V1 variant of SARS-CoV-2. *Cell Res.* **31**, 720–722 (2021).

46. Han, P. et al. Receptor binding and complex structures of human ACE2 to spike RBD from Omicron and Delta SARS-CoV-2. *Cell* **185**, 630–640.e610 (2022).

47. Dulin, D., Lipfert, J., Moolman, M. C. & Dekker, N. H. Studying genomic processes at the single-molecule level: introducing the tools and applications. *Nat. Rev. Genet.* **14**, 9–22 (2013).

48. Shang, J. et al. Cell entry mechanisms of SARS-CoV-2. *Proc. Natl Acad. Sci. USA* **117**, 11727–11734 (2020).

49. V'kovski, P., Kratzel, A., Steiner, S, Stalder, H. & Thiel, V. Coronavirus biology and replication: implications for SARS-CoV-2. *Nat. Rev. Microbiol.* 19, 155–170 (2020).

50. Michaud, W. A., Boland, G. M. & Rabi, S. A. The SARS-CoV-2 spike mutation D614G increases entry fitness across a range of ACE2 levels, directly outcompetes the wild type, and is preferentially incorporated into trimers. Preprint at *bioRxiv* https://doi.org/10.1101/2020.08.25.267500 (2020).

51. Jackson, C. B., Farzan, M., Chen, B. & Choe, H. Mechanisms of SARS-CoV-2 entry into cells. *Nat. Rev. Mol. Cell Biol.* **23**, 3–20 (2022).

52. Harvey, W. T. et al. SARS-CoV-2 variants, spike mutations and immune escape. *Nat. Rev. Microbiol.* **19**, 409–424 (2021).

53. Escalera, A. et al. Mutations in SARS-CoV-2 variants of concern link to increased spike cleavage and virus transmission. *Cell Host Microbe* **30**, 373–387.e377 (2022).

54. Ulrich, L. et al. Enhanced fitness of SARS-CoV-2 variant of concern Alpha but not Beta. *Nature* **602**, 307–313 (2022).

55. Buss, L. F. et al. Three-quarters attack rate of SARS-CoV-2 in the Brazilian Amazon during a largely unmitigated epidemic. *Science* **371**, 288–292 (2021).

56. Sun, K. et al. SARS-CoV-2 transmission, persistence of immunity, and estimates of Omicron's impact in South African population cohorts. *Sci. Transl. Med.* **14**, eabo7081 (2022).

57. Starr, T. N. et al. Deep mutational scanning of SARS-CoV-2 receptor binding domain reveals constraints on folding and ACE2 binding. *Cell* **182**, 1295–1310.e1220 (2020).

58. Liu, C. et al. The antibody response to SARS-CoV-2 Beta underscores the antigenic distance to other variants. *Cell Host Microbe* **30**, 53–68.e12 (2022).

59. Bayarri-Olmos, R. et al. Functional effects of receptor-binding domain mutations of SARS-CoV-2 B.1.351 and P.1 variants. *Front. Immunol.* **12**, 757197 (2021).

60. Mlcochova, P. et al. SARS-CoV-2 B.1.617.2 Delta variant replication and immune evasion. *Nature* **599**, 114–119 (2021).

61. Hu, J. et al. Increased immune escape of the new SARS-CoV-2 variant of concern Omicron. *Cell Mol. Immunol.* **19**, 293–295 (2022).

62. Ju, B. et al. Immune escape by SARS-CoV-2 Omicron variant and structural basis of its effective neutralization by a broad neutralizing human antibody VacW-209. *Cell Res.* **32**, 491–494 (2022).

63. Fan, Y. et al. SARS-CoV-2 Omicron variant: recent progress and future perspectives. *Sig. Transduct. Target Ther.* **7**, 141 (2022).

64. Planas, D. et al. Considerable escape of SARS-CoV-2 Omicron to antibody neutralization. *Nature* **602**, 671–675 (2022).

65. Li, B. et al. Viral infection and transmission in a large, well-traced outbreak caused by the SARS-CoV-2 Delta variant. *Nat. Commun.* **13**, 460 (2022).

Methods

All chemicals used were supplied by Carl Roth or Sigma-Aldrich, unless otherwise noted.

Cloning and protein construct design

Tethered ligand fusion proteins were created, expressed and purified as previously described[18]. Constructs for ACE2-linker-RBD of SARS-CoV-1 were designed in SnapGene version 4.2.11 (GSL Biotech) based on a combination of the ACE2 sequence[66] available from GenBank under accession number AB046569 and the SARS-CoV-1 sequence[67] available from GenBank under accession number AY274119. The crystal structure[68] available from the Protein Data Bank (PDB ID: 2ajf) was used as a reference. The linker sequence and tag placement were adapted from another work[69]. The linker sequence is a combination of two sequences available at the iGEM parts database (accession numbers BBa_K404300 and BBa_K243029). The fusion protein with the sequence of the RBD of SARS-CoV-2 was designed from the sequence published elsewhere[70] and available from GenBank under accession number MN908947, with a 6x histidine (His) tag added for purification. In addition, tags for specific pulling in MT and the AFM were introduced: a triple glycine for sortase-mediated attachment on the N terminus and a ybbR-tag, AviTag, and Fgγ tag on the C terminus. In summary, the basic construct is built up as follows: MGGG-ACE2-linker-RBD-6xHIS-ybbR-AviTag-Fgγ. All protein sequences are provided in the Supplementary Information.

The constructs were cloned using Gibson assembly from linear DNA fragments (GeneArt, Thermo Fisher Scientific) containing the codon-optimized sequence of choice for expression in *Escherichia coli* into a Thermo Scientific pT7CFE1-NHis-GST-CHA vector (product no. 88871). The mutations found in the VOCs causing amino acid substitutions in the RBD were introduced by blunt-end cloning and ligation. The replication of DNA plasmids was obtained by transforming in DH5-Alpha cells and running overnight cultures with 7 ml lysogeny broth with 50 µg ml^{-1} carbenicillin. Plasmids were harvested using a QIAprep Spin Miniprep Kit (QIAGEN, no. 27106).

In vitro protein expression

Expression was conducted according to the manual of 1-Step Human High-Yield Mini in vitro translation kit (no. 88891X) distributed by Thermo Fisher Scientific (Pierce Biotechnology). All of the components, except the 5× dialysis buffer, were thawed on ice until completely thawed. The 5× dialysis buffer was thawed for 15 min and 280 µl were diluted into 1,120 µl nuclease-free water to obtain a 1× dialysis buffer. The provided dialysis device was placed into the dialysis buffer and kept at room temperature until it was filled with the expression mix.

For preparing the in vitro translation expression mix, 50 µl of the HeLa lysate was mixed with 10 µl of accessory proteins. After each pipetting step, the solution was gently mixed by stirring with the pipette. Then, the HeLa lysate and accessory proteins mix was incubated for 10 min. Afterwards, 20 µl of the reaction mix was added. Then, 8 µl of the specifically cloned DNA (0.5 µg µl^{-1}) was added. The reaction mix was then topped off with 12 µl of nuclease-free water to obtain a total of 100 µl. This mix was briefly centrifuged at 10,000×*g* for 2 min. A small white pellet appeared. The supernatant was filled into the dialysis device placed in the 1× dialysis buffer. The entire reaction was then incubated for 16 h at 30 °C under constant shaking at 700 r.p.m. For incubation and shaking, a ThermoMixer comfort 5355 (Eppendorf, no. 5355) with a 2 ml insert was used. After 16 h, the expression mix was removed and stored in a protein low-binding reaction tube on ice until further use.

Protein purification

Purification was conducted using HIS Mag Sepharose Excel beads (Cytiva, no. 17371222) together with a MagRack 6 (Cytiva, no. 28948964) following the vendor's protocol. The bead slurry was thoroughly mixed by vortexing. Then, 200 µl of homogeneous beads were dispersed in a 1.5 ml protein low-binding reaction tube. Afterwards, the reaction tube was placed in the magnetic rack and the stock buffer was removed. Next, the beads were washed with 500 µl of HIS wash buffer (25 mM Tris-HCl, 300 mM NaCl, 20 mM imidazole, 10.00 vol.% glycerol, 0.25 vol.% Tween 20, pH 7.8). The expressed protein from in vitro transcription/translation was filled to 1,000 µl with Tris-buffered saline (25 mM Tris, 72 mM NaCl, 1 mM CaCl$_2$, pH 7.2) and mixed with freshly washed beads. The mix was incubated in a shaker for 1 h at room temperature. Subsequently, the reaction tube was placed in the magnetic rack and the liquid was removed. The beads were washed three times with the wash buffer, keeping the total incubation time to less than 1 min. The remaining wash buffer was removed and 100 µl elution buffer (25 mM Tris-HCl, 300 mM NaCl, 300 mM imidazole, 10.00 vol.% glycerol, 0.25 vol.% Tween 20, pH 7.8) were added to wash the protein off the beads. The bead elution buffer mix was then incubated for one minute with occasional gentle vortexing. Afterwards, the reaction tube was placed in the magnetic rack again to remove the eluted protein. This step was repeated for the second and third elution steps. The buffer of the eluted protein was exchanged to Tris-buffered saline in 0.5 ml 40k Zeba spin columns distributed by Thermo Fisher Scientific (Pierce Biotechnology, no. 87767) or 0.5 ml 50k Amicon Centrifugal Filters (Merck KGaA, no. UFC5050BK). Concentrations were photospectrometrically determined with NanoDrop and aliquots were frozen in liquid nitrogen.

MT instrument

Measurements were performed on a custom-built MT setup that has been described previously[20,71]. In the MT, the molecules are tethered between a flow-cell (FC) (see the 'FC preparation and MT measurements' section) surface and superparamagnetic beads (Dynabeads M-270 Streptavidin, Invitrogen, Life Technologies). Mounted above the FC is a pair of permanent magnets (5 × 5 × 5 mm^3 each; W-05-N50-G, Supermagnete) in the vertical configuration (34) with a 1 mm gap between the magnets. The distance between the magnets and FC is controlled by a d.c. motor (M-126.PD2, Physik Instrumente) and the FC is illuminated by a light-emitting diode (69647, Lumitronix LED Technik). Using a ×40 oil-immersion objective (UPLFLN 40×, Olympus) and a complementary metal–oxide–semiconductor sensor camera (5,120 × 5,120 pixels, CP80-25-M-72, Optronis), a field of view of approximately 680 × 680 µm^2 is imaged at a frame rate of 72 Hz. To control the focus and to create the look-up table required for tracking the bead positions in z, the objective is mounted on a piezo-stage (Pifoc P-726.1CD, Physik Instrumente). The images are read out with a frame grabber (microEnable 5 ironman VQ8-CXP6D, Silicon Software) and analysed with an open-source tracking software[72,73].

The tracking accuracy of our setup is ~1 nm in (x, y, z), as determined by tracking non-magnetic polystyrene beads, which were immobilized by baking them onto the FC surface. Force calibration was performed by measuring the transverse fluctuations of 21 kbp DNA tethers (described in another work[74]) for distances between the magnet and surface ranging from 0 to 10 mm (ref. 22) (Supplementary Fig. 2). The increase in transverse fluctuations with decreasing force for a DNA tether of known length is used to calculate the force calibration that relates the magnet height above the FC to the magnetic force on the bead[21,75]. Importantly, for the small extension changes on the length scales of our protein tethers, the force stays constant to a very good approximation during the extension of the tether and unfolding of the protein construct (to better than 10^{-4} relative change[20]). The largest source of force uncertainty is due to bead-to-bead variation, which is ≤10% for the beads used in this study[24,76].

FC preparation and MT measurements

FCs were prepared as described previously[20]. For the bottom slides, high-precision microscope cover glasses (24.00 mm × 60.00 mm × 0.17 mm, Carl Roth) were amino-silanized for further functionalization (equal to the AFM surface preparation).

They were coated with sulfosuccinimidyl 4-(*N*-maleimido-methyl) cyclohexane-1-carboxylate (sulfo-SMCC) (ref. 77) (Thermo Fisher Scientific, Pierce Biotechnology, no. 22322). For this purpose, 180 µl sulfo-SMCC (10 mM in 50 mM HEPES buffer, pH 7.4) was applied to one amino-silanized slide that was sandwiched with another slide and incubated for 45 min. Unbound sulfo-SMCC was removed by rinsing with Milli-Q water. Next, elastin-like polypeptide (ELP) linkers[25] with a sortase motif at their C terminus were coupled to the maleimide of the sulfo-SMCC via a single cysteine at their N terminus, by sandwiching two slides with 100 µl ELP linkers (in 50 mM disodium phosphate buffer with 50 mM NaCl and 10 mM EDTA, pH 7.2) and incubating them for 60 min. Subsequently, after further Milli-Q rinsing to remove the unbound ELP linkers, free sulfo-SMCC was neutralized with free cysteine (10 mM in 50 mM disodium phosphate buffer with 50 mM NaCl and 10 mM EDTA, pH 7.3). Thereafter, 1-µm-diameter polystyrene beads dissolved in ethanol were applied to the glass slides. After the ethanol evaporated, beads were baked onto the glass surface for 5 min at ~80 °C to serve as the reference beads during the measurement. FCs were assembled from an ELP-functionalized bottom slide and an unfunctionalized high-precision microscope cover glass slide with two holes (inlet and outlet) on either side serving as the top slide. Both slides were separated by a single layer of parafilm (Pechiney Plastic Packaging), which was cut out to form a 50 µl channel. FCs were incubated with 1% (v/v) casein solution (no. C4765-10ML, Sigma-Aldrich) for 2 h and flushed with 1 ml buffer (25 mM Tris, 72 mM NaCl, 1 mM CaCl2, pH 7.2, at room temperature).

CoA-biotin (no. S9351 (discontinued), New England Biolabs) was coupled to ybbR-tag at the C terminus of the fusion protein constructs in a 90–120 min bulk reaction in the presence of 4 µM sfp phosphopantetheinyl transferase[78] and 100 mM MgCl$_2$ at room temperature (~22 °C). Proteins were diluted to a final concentration of about 50 nM in 25 mM Tris, 72 mM NaCl, 1 mM CaCl$_2$, pH 7.2, at room temperature. To couple the N terminus of the fusion proteins carrying three glycines to the C-terminal LPETGG motif of the ELP linkers, 100 µl of the protein mix was flushed into the FC and incubated for 24 min in the presence of 1.3 µM evolved pentamutant sortase A from *Staphylococcus aureus*[79,80]. Unbound proteins were flushed out with 1 ml measurement buffer (25 mM Tris, 72 mM NaCl, 1 mM CaCl$_2$, 0.1% (v/v) Tween 20, pH 7.2). Finally, commercially available streptavidin-coated paramagnetic beads (Dynabeads M-270 Streptavidin, Invitrogen, Life Technologies) were added into the FC and incubated for 30 s before flushing out the unbound beads with 1 ml measurement buffer. Receptor–ligand binding and unbinding under force was systematically investigated by subjecting the protein tethers to 2–30-min-long plateaus of constant force, which was gradually increased in steps of 0.2 or 0.3 pN. All measurements were conducted at room temperature.

Data analysis of MT traces

MT traces were selected on the basis of the characteristic ACE2 two-step unfolding pattern above 25 pN, conducted at the end of each experiment. For each trace, (*x*, *y*) fluctuations were also checked to avoid the inclusion of tethers that exhibit interbead or bead–surface interactions, which would also cause changes in *x* or *y*. Non-magnetic reference beads were simultaneously tracked with magnetic beads and reference traces were subtracted for all measurements to correct for drift. Extension time traces were smoothed to one second with a moving-average filter to reduce noise. All analyses were performed with custom scripts in MATLAB.

MD simulations

To provide a complementary microscopic view of the RBD–ACE2 complex, we carried out MD simulations employing NAMD 3.0 (ref. 41). The simulations were prepared using VMD[81] and its QwikMD[82] interface. The structure of the complexes was prepared by following established protocols[83]. As the starting point, we used the crystallographic structure of the wt SARS-CoV-2 RBD–ACE2 complex from the protein data bank (PDB ID: 6m0j)[44]. The structure for the VOCs Alpha, Beta, Gamma, Delta and Omicron were obtained using MODELLER[40], with standard parameters and implementing the corresponding mutations described in the Supplementary Information. Omicron VOC model was constructed according to the following mutations found on RBD: G339D, S371L, S373P, S375F, K417N, N440K, G446S, S477N, T478K, E484A, Q493R, G496S, Q498R, N501Y, Y505H.

Employing advanced run options of QwikMD, structural models were solvated and the net charge of the proteins was neutralized using a 75 mM salt concentration of sodium chloride, which were randomly arranged in the solvent. All simulations were performed employing the NAMD MD package[41] and run on NVIDIA DGX-A100-based cluster nodes at Auburn University. The CHARMM force field[84,85] along with the TIP3 water model[86] was used for all systems. The simulations were performed with periodic boundary conditions in the NPT ensemble, with the temperature maintained at 300 K and pressure at 1 bar using Langevin dynamics. A distance cut-off of 12.0 Å was applied to short-range, non-bonded interactions, whereas long-range electrostatic interactions were treated using the particle mesh Ewald[87] method. The equations of motion were integrated using the reversible reference system propagator algorithm multiple time-step scheme[88] to update the van der Waals interactions every two steps and electrostatic interactions every four steps. The time step of integration was chosen to be 4 fs for all of the production simulations performed, and 2 fs for all of the equilibration runs. For the 4 fs simulations, hydrogen-mass repartitioning was done using psfgen in VMD. Before the MD simulations, all systems were submitted to an energy minimization protocol for 5,000 steps.

MD simulations with position restraints in the protein backbone atoms were performed for 1.0 ns and served to pre-equilibrate the systems before the 10.0 ns equilibrium MD runs, which served to evaluate the structural model stability. During the 1.0 ns pre-equilibration, the initial temperature was set to zero and was constantly increased by 1 K every 1,000 MD steps until the desired temperature (300 K) was reached. Production runs with no restraints on the system were performed for 200 ns, in five replicas, for each system, totalling 1 µs per system.

Analysis of MD simulations

Analyses of MD trajectories were carried out using Dynamical Network Analysis[42], using custom Python (Version 3.8) code and VMD[81] and its plug-ins. In the Dynamical Network Analysis[42], a network is defined as a set of nodes, and each node represents an amino acid residue. Each node's position is given by the residue's α-carbon. Edges connect pairs of nodes if their corresponding residues are in contact and two non-consecutive residues are said to be in contact if they are within 4.5 Å of each other for at least 75% of the analysed frames[42]. To ensure a broad sampling of our systems, each of the five 200 ns MD trajectories for each system were split in 5 ns windows, and only the last 15 windows, or 75 ns, were used for the analysis. Moreover, for the analysis of total correlation in RBD–ACE2 interfaces, we filtered out all contacts that presented an average correlation of motion smaller than 0.2 to reduce noise and remove weak transient interactions from the analysis.

Bootstrapping for CIs and significance testing

The CIs for the mean total correlation reported in Fig. 3e were determined using bootstrapping and the bias-corrected accelerated method[89], as implemented in SciPy[90]. The same method was used to determine the CIs presented in Supplementary Figs. 6 and 13, all of which were at a 90% confidence level.

To test if the total correlation distributions from distinct VOCs had significantly different means (Supplementary Fig. 13a), we used the non-parametric bootstrapping technique for hypothesis testing, with 10,000 samplings, as proposed in another work[89]. The same technique

was used on the experimental data for $F_{1/2}$ (Supplementary Fig. 6) and we obtained similar results as the parametric t-test.

Two-dimensional network of protein interface
The two-dimensional representation (Supplementary Fig. 10) was created by first mapping the three-dimensional positions of residues of the RBD near the RBD–ACE2 interface in the wt system to a two-dimensional space. This was done using a principal component analysis transformation as implemented in scikit-learn[91]. The plots were created using the interface between NetworkX[92] and matplotlib[93] in Python. The mean correlations were calculated as described above, and the CIs (Supplementary Fig. 10a) were calculated using the bias-corrected accelerated method for bootstrapping.

Data availability
Source data are provided with this paper. Additional data can be obtained from the corresponding author upon request.

Code availability
Code can be obtained from the corresponding author upon request.

References
66. Komatsu, T. et al. Molecular cloning, mRNA expression and chromosomal localization of mouse angiotensin-converting enzyme-related carboxypeptidase (mACE2). *DNA Sequence* **13**, 217–220 (2002).
67. Marra, M. A. et al. The genome sequence of the SARS-associated coronavirus. *Science* **300**, 1399–1404 (2003).
68. Li, F., Li, W., Farzan, M. & Harrison, S. C. Structure of SARS coronavirus spike receptor-binding domain complexed with receptor. *Science* **309**, 1864–1868 (2005).
69. Milles, L. F. & Gaub, H. E. Is mechanical receptor ligand dissociation driven by unfolding or unbinding? Preprint at *bioRxiv* https://doi.org/10.1101/593335 (2019).
70. Wu, F. et al. A new coronavirus associated with human respiratory disease in China. *Nature* **579**, 265–269 (2020).
71. Walker, P. U., Vanderlinden, W. & Lipfert, J. Dynamics and energy landscape of DNA plectoneme nucleation. *Phys. Rev. E* **98**, 042412 (2018).
72. van Loenhout, M. T., Kerssemakers, J. W., De Vlaminck, I. & Dekker, C. Non-bias-limited tracking of spherical particles, enabling nanometer resolution at low magnification. *Biophys. J.* **102**, 2362–2371 (2012).
73. Cnossen, J. P., Dulin, D. & Dekker, N. H. An optimized software framework for real-time, high-throughput tracking of spherical beads. *Rev. Sci. Instrum.* **85**, 103712 (2014).
74. Lipfert, J. et al. Methods and protocols. *Methods Mol. Biol.* **582**, 71–89 (2009).
75. Yu, Z. et al. A force calibration standard for magnetic tweezers. *Rev. Sci. Instrum.* **85**, 123114 (2014).
76. De Vlaminck, I., Henighan, T., van Loenhout, M. T., Burnham, D. R. & Dekker, C. Magnetic forces and DNA mechanics in multiplexed magnetic tweezers. *PLoS ONE* **7**, e41432 (2012).
77. Zimmermann, J. L., Nicolaus, T., Neuert, G. & Blank, K. Thiol-based, site-specific and covalent immobilization of biomolecules for single-molecule experiments. *Nat. Protoc.* **5**, 975–985 (2010).
78. Yin, J., Lin, A. J., Golan, D. E. & Walsh, C. T. Site-specific protein labeling by Sfp phosphopantetheinyl transferase. *Nat. Protoc.* **1**, 280–285 (2006).
79. Chen, I., Dorr, B. M. & Liu, D. R. A general strategy for the evolution of bond-forming enzymes using yeast display. *Proc. Natl Acad. Sci. USA* **108**, 11399–11404 (2011).
80. Durner, E., Ott, W., Nash, M. A. & Gaub, H. E. Post-translational sortase-mediated attachment of high-strength force spectroscopy handles. *ACS Omega* **2**, 3064–3069 (2017).
81. Humphrey, W., Dalke, A. & Schulten, K. VMD: visual molecular dynamics. *J. Mol. Graph.* **14**, 33–38 (1996).
82. Ribeiro, J. V. et al. QwikMD—integrative molecular dynamics toolkit for novices and experts. *Sci. Rep.* **6**, 26536 (2016).
83. Bernardi, R. C. et al. Mechanisms of nanonewton mechanostability in a protein complex revealed by molecular dynamics simulations and single-molecule force spectroscopy. *J. Am. Chem. Soc.* **141**, 14752–14763 (2019).
84. Best, R. B. et al. Optimization of the additive CHARMM all-atom protein force field targeting improved sampling of the backbone ϕ, ψ and side-chain χ_1 and χ_2 dihedral angles. *J. Chem. Theory Comput.* **8**, 3257–3273 (2012).
85. MacKerell, A. D. et al. All-atom empirical potential for molecular modeling and dynamics studies of proteins. *J. Phys. Chem. B* **102**, 3586–3616 (1998).
86. Jorgensen, W. L., Chandrasekhar, J., Madura, J. D., Impey, R. W. & Klein, M. L. Comparison of simple potential functions for simulating liquid water. *J. Chem. Phys.* **79**, 926–935 (1998).
87. Darden, T., York, D. & Pedersen, L. Particle mesh Ewald: an $N \cdot \log(N)$ method for Ewald sums in large systems. *J. Chem. Phys.* **98**, 10089–10092 (1993).
88. Phillips, J. C. et al. Scalable molecular dynamics with NAMD. *J. Comput. Chem.* **26**, 1781–1802 (2005).
89. Efron, B. & Tibshirani, R. J. *An Introduction to the Bootstrap* 372–391 (CRC Press, 1994).
90. Virtanen, P. et al. SciPy 1.0: fundamental algorithms for scientific computing in Python. *Nat. Methods* **17**, 261–272 (2020).
91. Pedregosa, F. et al. Scikit-learn: machine learning in Python. *J. Mach. Learn. Res.* **12**, 2825–2830 (2011).
92. Hagberg, A. A., Schult, D. A. & Swart, P. J. ExplorkX. In *Proc. 7th Python in Science Conference* https://www.osti.gov/servlets/purl/960616 (2008).
93. Hunter, J. D. Matplotlib: a 2D graphics environment. *Comput. Sci. Eng.* **9**, 90–95 (2007).

Author contributions
M.S.B., S.G., A.H., M.C.R.M., P.S.F.C.G., H.E.G., R.C.B. and J.L. designed the research. M.S.B., S.G. and A.H. built the instruments and performed the experiments. P.S.F.C.G., M.C.R.M. and R.C.B. performed and analysed the simulations. M.S.B., S.G., A.H., L.F.M. and T.N. contributed the new reagents and analytic tools. M.S.B., S.G. and A.H. analysed the experimental data. M.S.B., S.G., A.H., M.C.R.M., P.S.F.C.G., H.E.G., R.C.B. and J.L. wrote the paper with input from all authors.

Competing interests
The authors declare no competing interests.

Additional information